Surface reconstructions and melting of CaF_2 surfaces

Somayeh Faraji,[1] S. Alireza Ghasemi,[1,*] Behnam Parsaeifar,[2] and Stefan Goedecker[2]
[1] *Institute for Advanced Studies in Basic Sciences, P.O. Box 45195-1159, Zanjan, Iran*
[2] *Department of Physics, Klingelbergstrasse 82, 4056 Basel, Switzerland*

(Dated: February 28, 2019)

In the present work, surface reconstructions of CaF_2 in three different low-index crystallographic orientations are comprehensively investigated. The configurational spaces were explored by employing the minima hopping method (MHM) and the machine-learning based potential founded on charge equilibration via neural network technique (CENT). The cooperation of these powerful methods revealed more than 80 different morphologies for (100) surface with very close surface formation energies in the energy difference range about 0.3 J/m^2. This finding indicates the high mobility of the atoms positioned at the outer layers, making it a very dynamic surface. To consider the effect of temperature on the dynamic of this surface as well as study the solid-liquid transformation, the molecular dynamics simulations were carried out in the canonical (N,V,T) ensemble. By considering mean-squared displacements (MSD) of layers and elements of this sample at the temperature range of 273.15-1500 K, it was recognized that the F sublattice is less stable and more dynamics than the Ca sublattice, resulting in surface pre-melting at temperatures lower than the one for bulk phases.

I. INTRODUCTION

Special chemical and physical properties of alkaline halide crystals have raised a lot of attention, making them the subject of intense scientific research. Calcium fluoride (CaF_2), crystallized in fluorite structure, is one of the most archetypal alkali fluorides with special properties such as high band gap and high melting and boiling temperature. The melting temperature of this compound was firstly predicted theoretically[1] about 1665 K and then was reported experimentally[2] about 1675 K. Its high melting point along with excellent physical and optical properties such as a wide range of light transmission in both ultraviolet and infrared ranges, high laser damage threshold and superwide bandgap (12 eV) have made it an special candidate to find applications in optical windows, prisms and main lens substrate candidate for large-scale semiconductor micro-lithography systems, micro-resonator fabrication and photodetectors. [3–8] In such applications, shape precision, surface morphology, hardness, the smoothness of CaF_2 surfaces as well as the dependency of them on the crystallographic orientation are very important. Consequently, the surfaces of this material have been the subject of numerous experimental and theoretical studies to investigate the structure and morphology of the surfaces. [9–21] Experimentally, the insulating behavior of alkaline halide surfaces hampers surface studies with electron probe beams and scanning tunneling microscopy.[22] Therefore, low-energy electron diffraction (LEED) [23,24], X-ray diffraction[25] and atomic force microscopy (AFM) [26] are the experimental techniques well suited to study the structure of such surfaces. Beside such experimental techniques, computational and theoretical studies also have provided accurate results for such surfaces. As an example of such studies, Puchin *et al*[10] performed a systematic theoretical investigation of various surfaces with respect to their relative stabilities and the effect of surface relaxation/reconstruction on bandgaps. Fisicaro, *et al.* performed extensive structure prediction calculations with the MHM[27,28] to compare the stability of hydrated (100) and (111) surfaces, giving insight into different experimentally observed morphologies in CaF_2 nanocrystals[29] According to these studies, the CaF_2 surfaces exhibit strong anisotropy based on the crystallographic orientations, e.g. experimental studies to consider the effect of increasing temperature on typical anisotropy in the Knoop hardness of (001) and (111) planes have confirmed that it decreases uniformly on both planes and there is a little change in the anisotropy and the hardness of (001) plane is higher than (111).[30]

In addition to such extensive studies on CaF_2 surfaces and available information in the literature, it is also useful to have knowledge of the ionic dynamics, collective behavior and melting of the surfaces of this material and looking for the thermal behaviour of different surface orientation as the temperature varies. Besides, to provide deeper understanding of surface-related phenomena and refinements in experimental techniques and technological applications, it is also worthful to provide knowledge of the arrangement of the ions in the topmost layers and their thermal behaviors. To aim these goals, tensor LEED analyses [12,15] have been successfully applied on CaF_2 (111), to obtain parameters such as mean-squared displacements (MSD) of layers and elements which are also accessible by molecular dynamics (MD) simulations.

In spite of these experimental researches on CaF_2 (111) surfaces, there is no theoretical or experimental study to investigate the effect of temperature on other orientations of the surfaces. Furthermore, surface morphologies of different orientations, solid-liquid transformation processes, and melting behaviors are in general important phenomena in nature which having detailed knowledge of them has great importance for engineers, materials designer and geophysics for a long time. Therefore, all of these make motivation to convey researches in these fields.

The present study consists of two parts. The first part is the exploration of the potential energy surfaces (PES) of three low-index surfaces of CaF_2 by employing minima hopping method (MHM)[27,28] and charge equilibration neural network technique (CENT) [31,32] for which the accuracy and transferability was demonstrated in our previous work[32]. The found surface morphologies were also validated by doing DFT calculations in order to find their stability at this level. In the second part, we investigate premelting and melting of the (100) surface by employing CENT potential and doing MD simulations in the temperature range between 300 and 1500 K and using Nose' Hoover thermostat as implemented in LAMMPS.[33] Before doing the second part, the potential was evaluated by doing MD simulation of bulk and (111) surface and comparing the results with available experimental and theoretical results in the literature.

II. METHODS

A. Surface geometries and reconstructions

Three low-index slabs, namely (111), (110), and (100), for which the atomic arrangements are illustrated in Fig. 1 were cut out from the fully relaxed bulk of CaF_2 in fluorite phase with equilibrium lattice constant of 5.483 Å. For each of the samples, the surface reconstructions were explored by employing MHM which is an efficient algorithm to explore the energy landscape of a system by performing consecutive MD escape steps followed by doing local geometry optimization. To accelerate the exploration of the energy landscape it exploits the Bell-Evans-Polanyi principle for the moves from one funnel to another one by aligning the initial MD velocities preferably along soft mode directions. Beside that, there is a built-in feedback mechanism to avoid trapping in a funnel or revisiting known parts of the configurational space. Multiple MHM structure prediction runs were performed starting from different initial surface structures in conjunction with the CENT potential while the three bottom layers were fixed in their atomic positions. This potential which is a neural-network based technique was developed based on the distribution of the electronic charge density determined by atomic environment-dependent electronegativities. This procedure allows to provide accurate description of the energetics of ionic systems in which long-range charge transfer or ionization is important.[31] To train the CENT potential, as completely explained in our previous work[32], a database containing the DFT energies of about 2800 charge-neutral cluster structures were prepared with sizes ranging from 24 to 99 atoms. These structures were generated iteratively, starting from an approximate potential obtained by fitting CENT to DFT data of randomly generated structures in an initial step. Subsequently, further structures were added to the training set by performing MHM simulations with the approximate potential and filter them carefully to avoid duplicate structures and being ensure about diversity in structural motifs. This filtering was done by comparing structures with a structural fingerprint.[34] This procedure was repeated several times until a desired accuracy of was reached for a predefined validation data set. To solve the Poisson's equation with surface boundary conditions, the P^3D method was used without the need to introduce vacuum region in the nonperiodic dimensions. Among the three surfaces, the (100) surface is a polar surface consisting of oppositely charged planes. Therefore, 50% of the fluorine atoms were moved from the top of the slab to the bottom to suppress the dipole moment. It is well known that a limited size of the simulation cell can affect the correlation between particles of the system, resulting in serious drawbacks to the results. To overcome this problem and reducing the effect of cross section confinement, the larger supercells were also tested for the slabs with smaller surface cross sections. Table I summarizes the geometric characteristics of the examined surfaces.

TABLE I. The geometric characteristics of the considered supercells containing N atoms in the sample with thickness d (in Å) and cross section area A (in $Å^2$). a and b show the size of the supercell in the periodic directions along with a-axis and b-axis (in Å).

surface	N	a	b	A	d
(111)	288	15.5	13.4	207.7	17.6
(110)	144	11.6	11	127.6	13.6
(110)	576	23.3	21.9	510.3	13.6
(100)	72	7.8	7.8	60.8	16.5
(100)	144	11.1	11.1	123.2	16.5
(100)	324	16.6	16.6	275.6	16.5

Since, unlike the (100) surface which exhibited a plethora of reconstructions, the (111) and (110) did not show any significant change in their surface patterns, the (100) orientation was found more attractive to put it in the centre of the further consideration. Beside that, previously studies on the effect of polar and neutral aqueous solvent on the formation of these three facets of CaF_2 have demonstrated that the interaction with such environments promotes the formation of (100) facets by reducing the surface energy of (100) reconstructions while the surface reconstructions of (100) remain unchanged.[29,35] Therefore, among the (100) surface reconstructions, different patters with lowest energies per atom were selected and were relaxed by allowing all the atoms to move to be sure the fixed bottom atoms in the previous exploration has no effect on their stability. After the relaxation, the second step of selection was done based on the energy and patterns. Then, 85 different surface patterns were selected and symmetrized in a way both sides of the surface have the same patterns. To do such symmetrizing, all the layers above the central Ca layer were reflected around this layer (resulting in increasing the thickness

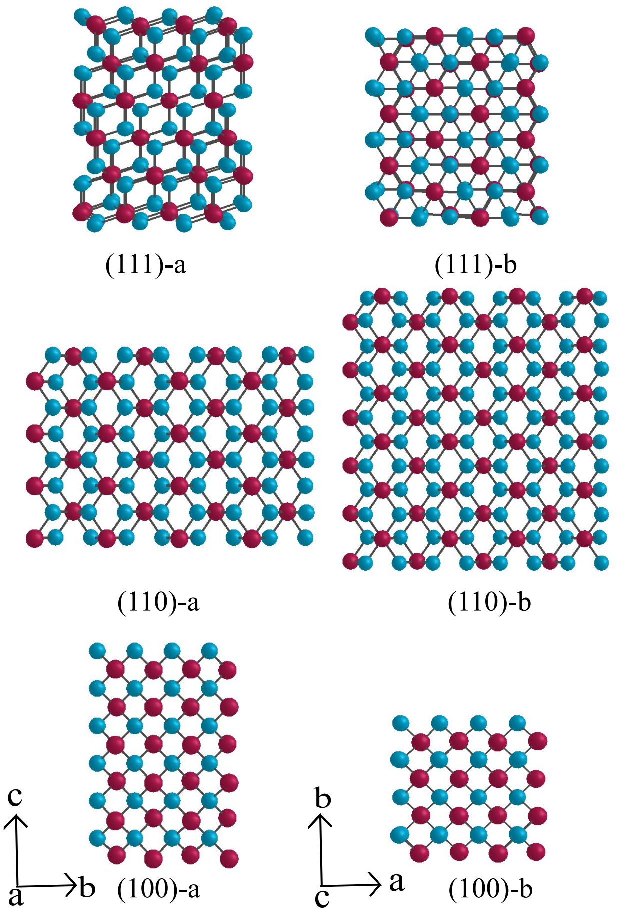

FIG. 1. (color online) Three different low-index surfaces of CaF_2 shown from the side along the a-axis (denoted by a) and the top along the c-axis (denoted by b) after a local relaxation. The blue and dark-purple spheres denote F and Ca atoms, respectively.

of slabs). For these symmetrized surfaces, the surface formation energy E_f defined as the work required to separate a crystal into two parts along a certain plane (100) were calculated according to

$$E_f = \frac{1}{2A}(E_s - nE_b), \qquad (1)$$

where A is the surface area, E_s is the total energy of the equilibrium structure of the slab, E_b is the bulk total energy per formula unit, and n is the number of f.u. in the slab. The factor $\frac{1}{2}$ accounts for the presence of two surfaces at either side of the slab.

To compare the results and validate them with DFT, the found surface reconstructions were optimized by applying Perdew-Burke-Ernzerhof (PBE)[36] exchange-correlation functional as implemented in the BigDFT package[37–39]. This package takes advantage of the localized basis functions based on wavelets, allowing perform electronic calculations for surface boundary condition without the need for introducing the vacuum region in nonperiodic directions. HOW TO EXPLANE THE TYPE OF PSEUDOPOTENTIAL WHICH WE USED HERE? To obtain the equilibrium lattice constant of bulk, the calculations were carried out by setting a uniform mesh with grid spacing of 0.33, 0.33, and 0.33 Bohr for the wavelet basis functions as well as a 4×4×4 k-point mesh to obtain energy convergence within 1 meV/atom. Then, the atomic positions and supercell sizes were scaled to the equilibrium lattice constant of bulk phase which was obtained 5.53 Å. The electronic structure calculations for the surfaces were done by setting the grid spacing of 0.3, 0.35, 0.3 Bohr and 3 × 1 × 3 and 2 × 1 × 2 k-point mesh for the smaller and larger supercells, respectively. All the atoms were allowed to move during the relaxation until the maximum force component was less than 5 meV/ Å.

B. MD simulations

By increasing temperature and approaching into the melting value of a solid, the lattice defects, mainly in type of Frenkel defects, will activate thermally and reach to high concentrations. In this state, the structure becomes closer to that of the liquid via continuously increasing disorder, phenomena generally known an premelting and melting transitions. To study such transitions, there are two main points. First point is a need for models to include the interaction of defects. There are a few simple empirical and semi-empirical models in which such interactions are included, however, they have been deficient in describing such phenomena accurately and correctly. [40] Second point is growing the correlation between particles of the system as temperature increases. These correlations are important when system is going through phase transition and a limited size of the simulation cell results in serious drawbacks, especially when periodic boundary condition is employed. To resolve these two problems, atomistic MD simulations, which unlike the (semi-) empirical models are able to work better, a long with larger simulation cells can be applied for such studies. In general, along with available experimental and theoretical techniques, MD simulations have been largely used to investigate a wide range of condensed matter phenomena, such as equilibrium structures, the structure and dynamics of solid surfaces, phase transformations, and thermal behaviors. Therefore, they are important tools to provide basic understanding of material processes and enrich our knowledge of the underlying energetics, fundamental interactions, and transformation mechanisms on a microscopic level. The main ingredients of the MD approaches are the interatomic interaction potential and molecular forces. Although these can be obtained from *ab initio* electronic structure calculations, the expensive computational perspective of them makes them only applicable for relatively small systems and short time simulations. In order to be able to investigate the system in larger supercells as well as provide accurate and fast evaluation of the energy and forces during the MD simulations, we also employed the CENT potential in this part of study. Since in our previous study the accuracy of the produced potential had not been tested for nonzero temperatures, at first we examined the bulk and (111) surface of $\mathrm{CaF_2}$ and compared our results with available studies in literatures. The MD simulations of a bulk supercell containing 324 atoms at temperatures 1100, 1200, 1400, and 1500 K where performed in the canonical (N,V,T) ensemble by employing Nose-Hoover thermostat as implemented in LAMMPS.[33] To be able to do this step, we made interface between our home-made code and LAMMPS to have access to its functionalities. The MD simulations were performed using periodic boundary condition, and a timestep of 0.5 fs and the temperature was kept fluctuating around a set-point value by using the mentioned thermostat and defining the value of 100 (in time units) for T_{damp}. All the atoms were allowed to move during the simulation and the velocities were initialized by a gaussian distribution with a mean of 0.0 and a sigma scaled to produce the requested temperature. At each temperatures, the size of the simulation cell was modified and updated by employing the thermal expansion coefficient of CaF_2 as[41]

$$\alpha(T) = 1.885\times10^{-5}+1.67\times10^{-8}(T-T_0)+5.5\times10^{-12}(T-T_0)^2 \tag{2}$$

MD simulations of the (111) surface for a supercell containing 576 atoms were also done with the same setting as described for the bulk phase.

After the evaluation of the CENT potential at numerous temperatures and establishing its good performance, it was employed for the (100) surface MD simulations. To do this, a larger supercell containing 480 atoms was prepared and the lattice constants and atomic positions at each temperature were rescaled according to Eq. 2 The MD simulations of the samples were carried out in a wide range of temperatures of 300-1500 K. The same setting of bulk MD simulations were also applied here except applying larger time step of 0.7 fs.

III. NUMERICAL RESULTS

A. Surface reconstructions

As explained in Sec. II, 85 different surface reconstructions were selected and symmetrized for doing final relaxations with CENT as well as their validation with DFT. The final 85 supercells, as shown in Figs 2- 5, containing symmetrized surfaces with 84 and 168 atoms were rerelaxed and the final relaxed structures were examined carefully to be sure they are not changed. From these 85 surface patterns, we found five of them were already reported by Fisicaro *et al*[29] (the structures marked by asterisk in column denoted by ID^{CENT} in Table II). In that study, the sampling of the configurational space was done by employing MHM in conjunction with DFT calculations. It is clear that electronic structure calculations based on DFT are computationally expensive, preventing extensive exploration of different parts of the PES to find different low-energy reconstructions. However, the CENT potential is not computationally costly, resulting in doing force and energy evaluations in a very shorter time. Therefore, employing MHM in conjunction with this potential have enabled us to do vast search over the energy landscape of (100) surfaces and obtain much more surface reconstructions than those presented there. Finally, these reconstructions were relaxed with DFT as was described in Sec. II According to our accurate analyses, nine of the surface patterns were changed. These structures are written bold in Table II). From these nine changed reconstructions, six of them were changed to others while three of which represented new ones. These three new reconstructions are shown in the last row of the Fig 5. The one labeld with new1 in that figure can be also found among the reconstructions reported by Fisicaro *et al.*

For each reconstruction, the surface formation energy was obtained by employing the Eq.1 as listed in Table II. Based on data in Table II, the E_fs are in the small range of 0.926 - 1.249 Jm^{-2}, demonstrating the high mobility of the outer atoms in the surface and the dynamic characteristics of it. Furthermore, according to our analyses, the energetic ordering of the surface reconstructions obtained by DFT were different from the CENT potential. Such changing in the energetic ordering is not surprising by regarding the point that even DFT calculations based on different applied XC functionals result in different ordering of stability. To simplify comparison of CENT and PBE results and make it more recognizable from the table, the order of stabilities according to DFT calculations is written as superscript near to the values in column E_{surf}^{DFT}. Both CENT and DFT represent surface energies which span a range of about 0.3 $\mathrm{J/m^2}$ (difference between the highest and lowest values of E_{surf}. Based on the CENT energies, the five stable structures with the lowest values for E_f are s01, s02, s03, s04, and s05 with 2.16%, 2.27%, 2.27%, and 2.48% higher in energy with respect to the s01. According to the DFT energies, the five stable structures with the lowest values for E_f are s04, s47, s05, s64, and s02 with 3.85%, 4.67%, 5.50%, and 5.5% higher in energy with respect to the lowest energy, s04.

B. Evaluation of the potential

To evaluate the performance of the potential for nonzero temperatures, two simulations sets were examined.

The first one was done for the bulk phase. It is well known that above a certain critical temperature, a large fraction of fluorine ions in the bulk phase of this material

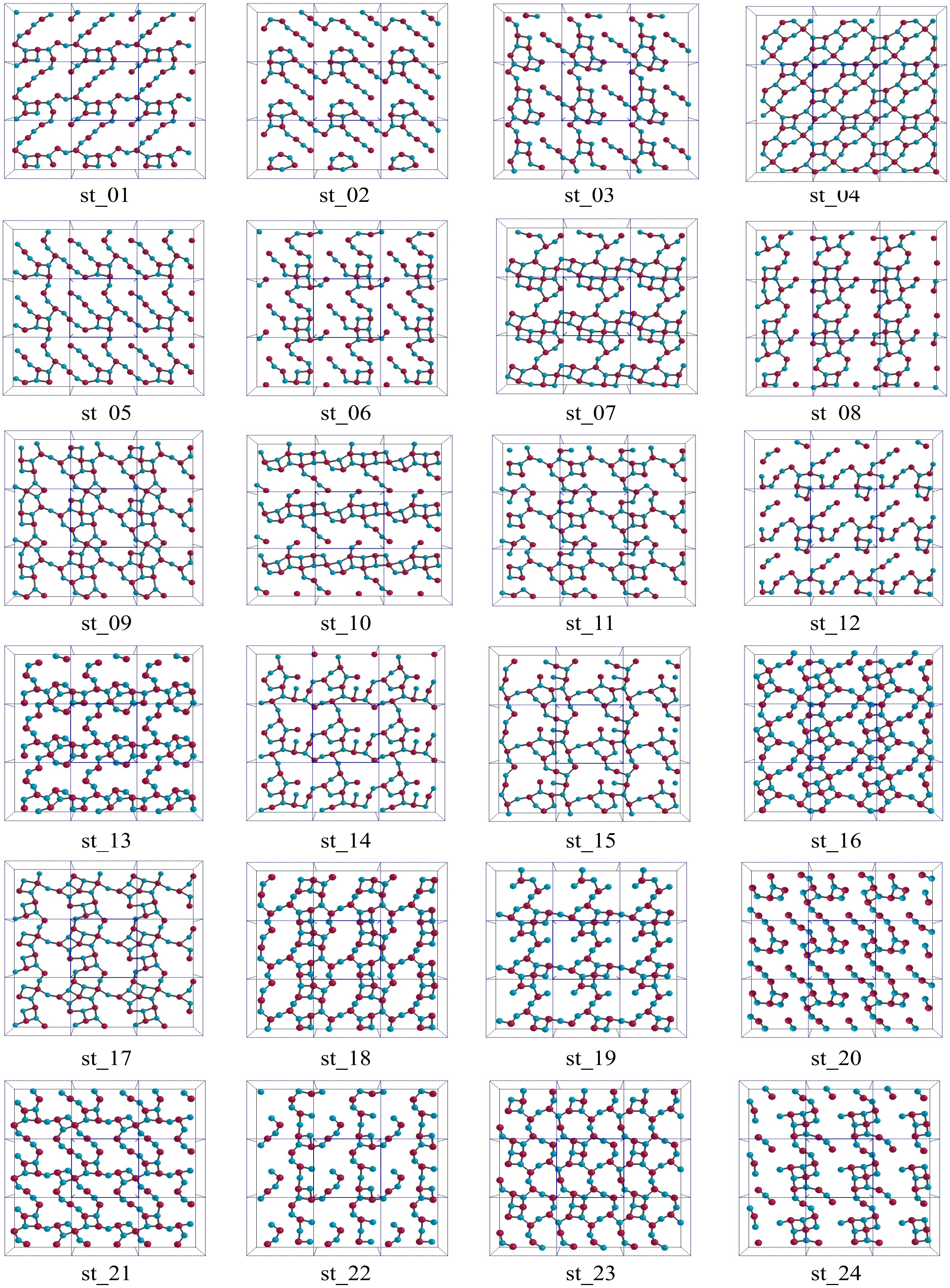

st_01 st_02 st_03 st_04

st_05 st_06 st_07 st_08

st_09 st_10 st_11 st_12

st_13 st_14 st_15 st_16

st_17 st_18 st_19 st_20

st_21 st_22 st_23 st_24

FIG. 2. Top view of the (100) reconstructed surfaces of CaF_2, ordered from the lowest surface formation energy. F and Ca atoms are denoted by blue and dark-purple spheres. (part 1)

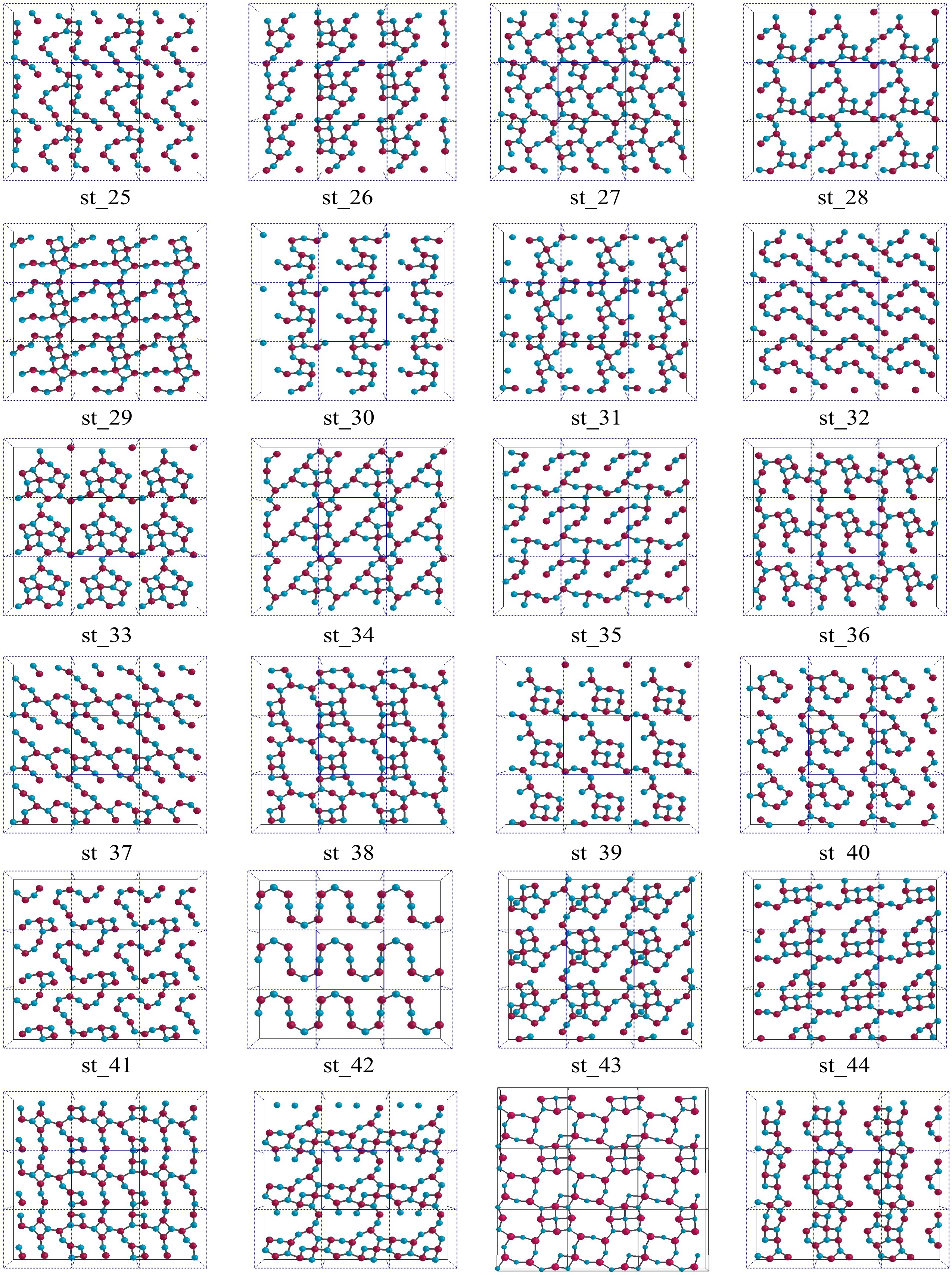

st_25 st_26 st_27 st_28

st_29 st_30 st_31 st_32

st_33 st_34 st_35 st_36

st_37 st_38 st_39 st_40

st_41 st_42 st_43 st_44

st_45 st_46 st_47 st_48

FIG. 3. Top view of the (100) reconstructed surfaces of CaF_2, ordered from the lowest surface formation energy. F and Ca atoms are denoted by blue and dark-purple spheres. (part 2)

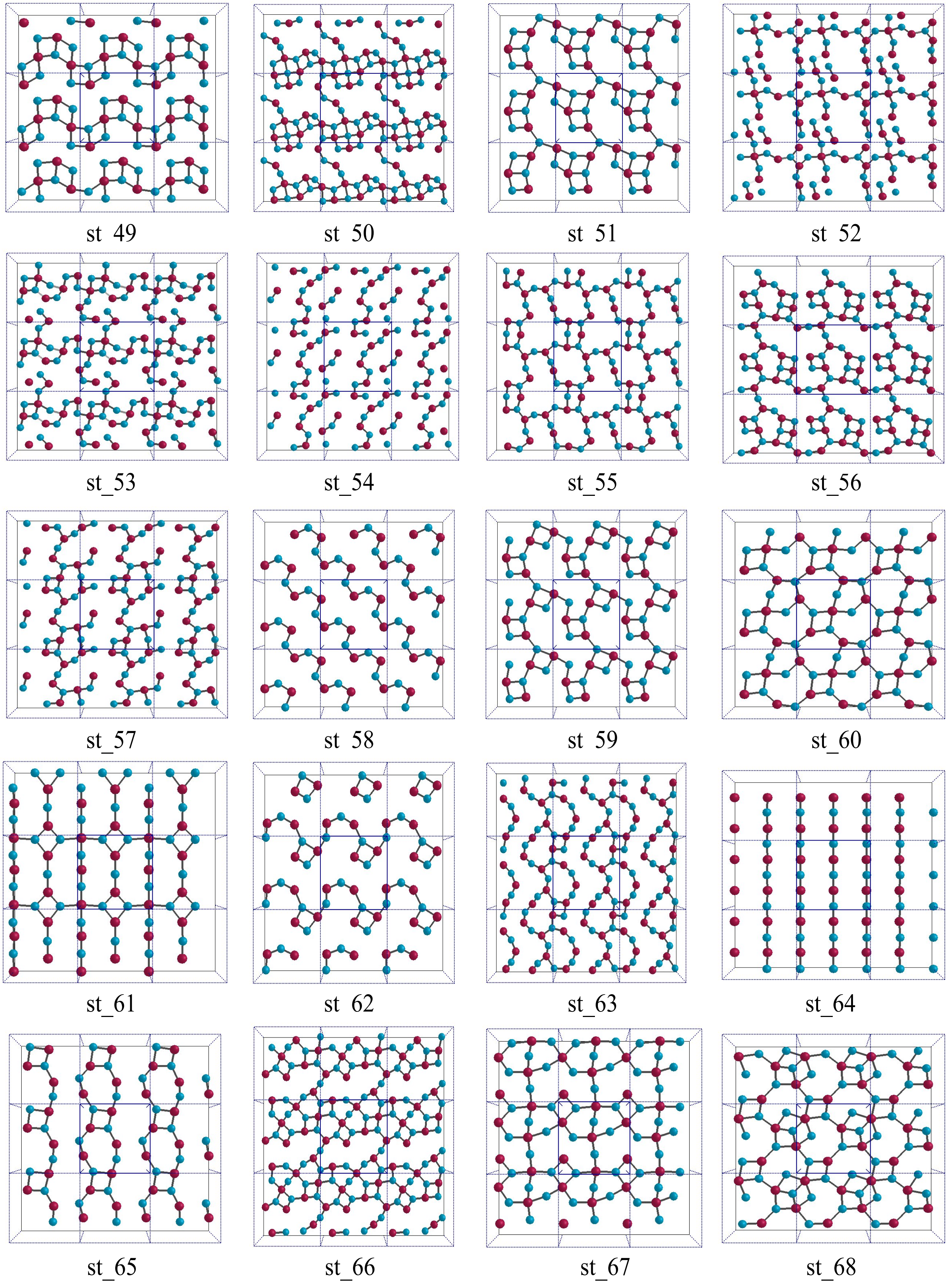

st_49 st_50 st_51 st_52

st_53 st_54 st_55 st_56

st_57 st_58 st_59 st_60

st_61 st_62 st_63 st_64

st_65 st_66 st_67 st_68

FIG. 4. Top view of the (100) reconstructed surfaces of CaF_2, ordered from the lowest surface formation energy. F and Ca atoms are denoted by blue and dark-purple spheres. (part 3)

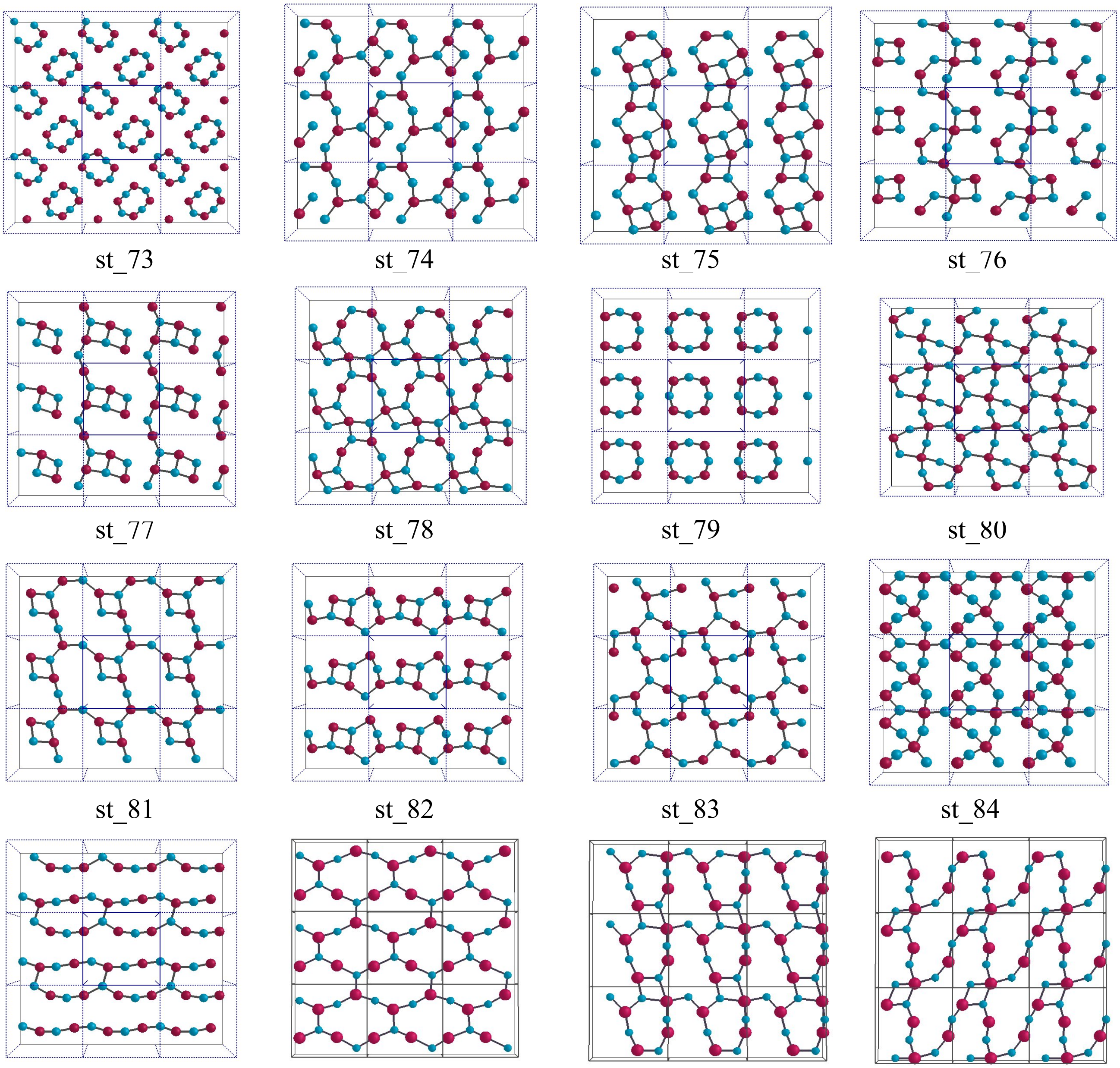

st_73 st_74 st_75 st_76

st_77 st_78 st_79 st_80

st_81 st_82 st_83 st_84

st_85 new1 new2 new3

FIG. 5. Top view of the (100) reconstructed surfaces of CaF_2, ordered from the lowest surface formation energy. F and Ca atoms are denoted by blue and dark-purple spheres. (part 4). The last three structures are the new surface reconstructions after doing relaxation by DFT.

TABLE II. Surface formation energies (E_f) in Jm^{-2} obtained from CENT potential and DFT calculations. N denotes the number of atoms in each sample. The columns labled with ID are according to the top views shown in figures 2- 5. The table is organized according to order of sability in CENT potential. Numbers written in the superscript of the E_f^{DFT} column determine the order of stability according to DFT calculations. The previously recognized patterns by Fisicaro *et al*[29] are also marked by asterrisk.

N	ID^{CENT}	ID^{DFT}	E_f^{CENT}	E_f^{DFT}	N	ID^{CENT}	ID^{DFT}	E_f^{CENT}	E_f^{DFT}	N	ID^{CENT}	ID^{DFT}	E_f^{CENT}	E_f^{DFT}
168	s01	s01	0.926	0.771^{6}	168	s30	s30	0.984	0.846^{52}	84	s59	s59	1.035	0.901^{70}
168	s02	s02	0.946	0.768^{5}	168	s31	s31	0.986	0.822^{36}	84	s60	s60	1.039	0.865^{62}
168	s03	s03	0.947	0.820^{35}	168	s32	s32	0.987	0.795^{16}	84	s61	s61	1.042	0.810^{24}
168	s04*	s04*	0.947	0.728^{1}	168	s33	s33	0.987	0.848^{55}	84	s62	s62	1.046	0.900^{68}
168	s05	s05	0.949	0.762^{3}	168	s34	s34	0.988	0.830^{44}	168	s63	s63	1.055	0.859^{59}
168	s06	s06	0.958	0.812^{27}	168	**s35**	s05	0.988	0.762^{3}	84	s64*	s64*	1.061	0.768^{4}
168	s07	s07	0.958	0.801^{18}	168	s36	s36	0.990	0.868^{63}	84	**s65**	s85	1.062	0.837^{50}
168	s08	s08	0.960	0.812^{26}	168	s37	s37	0.991	0.790^{14}	168	s66	s66	1.065	0.851^{56}
168	s09	s09	0.961	0.814^{28}	168	s38	s38	0.992	0.801^{19}	84	s67	s67	1.066	0.880^{65}
168	s10	s10	0.962	0.824^{38}	168	s39	s39	0.996	0.818^{33}	84	**s68**	new2	1.074	0.901^{69}
168	s11	s11	0.963	0.814^{29}	168	s40	s40	0.997	0.817^{32}	84	s69*	s69*	1.075	0.827^{42}
168	s12	s12	0.964	0.824^{37}	168	s41	s41	0.999	0.830^{45}	84	s70	s70	1.076	0.930^{74}
168	s13	s13	0.965	0.815^{30}	84	s42*	s42*	0.999	0.786^{13}	84	s71	s71	1.085	1.012^{81}
168	s14	s14	0.966	0.772^{8}	168	s43	s43	1.001	0.856^{57}	84	s72	s72	1.086	0.889^{67}
168	s15	s15	0.966	0.772^{7}	168	s44	s44	1.002	0.862^{61}	168	**s73**	s79*	1.090	0.845^{51}
168	s16	s16	0.966	0.775^{11}	168	s45	s45	1.003	0.837^{49}	84	**s74**	s04*	1.094	0.728^{1}
168	s17	s17	0.966	0.772^{9}	168	s46	s46	1.005	0.803^{21}	84	**s75**	s04*	1.100	0.728^{1}
168	s18	s18	0.968	0.825^{39}	168	s47	s47	1.009	0.756^{2}	84	s76	s76	1.102	1.004^{78}
168	s19	s19	0.969	0.791^{15}	168	s48	s48	1.010	0.889^{66}	84	s77	s77	1.102	0.964^{75}
168	s20	s20	0.972	0.802^{20}	84	**s49**	new1*	1.011	0.809^{22}	84	s78	s78	1.107	0.906^{71}
168	s21	s21	0.972	0.785^{12}	168	s50	s50	1.013	0.846^{53}	84	**s79***	new3	1.107	1.009^{79}
168	s22	s22	0.973	0.833^{48}	84	s51	s51	1.017	0.846^{54}	84	s80	s80	1.158	0.912^{72}
168	s23	s23	0.975	0.830^{46}	168	s52	s52	1.017	0.833^{47}	84	**s81**	s82	1.162	1.038^{82}
168	s24	s24	0.978	0.817^{31}	168	s53	s53	1.018	0.873^{64}	84	s82	s82	1.176	0.928^{73}
168	s25	s25	0.980	0.800^{17}	168	s54	s54	1.018	0.858^{58}	84	s83	s83	1.186	0.971^{76}
168	s26	s26	0.981	0.828^{43}	168	s55	s47	1.026	0.774^{10}	84	s84	s84	1.217	1.003^{77}
168	s27	s27	0.982	0.826^{41}	168	s56	s56	1.027	0.819^{34}	84	s85	s85	1.249	1.011^{80}
168	s28	s28	0.982	0.812^{25}	168	s57	s57	1.028	0.826^{40}					
168	s29	s29	0.983	0.809^{23}	84	s58	s58	1.031	0.862^{60}					

leave their ideal crystalline positions, and while obtaining high mobility comparable to that of a molten salt, they occupy interstitial places. In this circumstance which occurs below the melting temperature (T_m), the less stable fluorine sublattice is transformed into a sort of liquid, penetrating into the quasiperfect, more stable calcium sublattice. So, before the order-disorder transition temperature, there is still a recognizable well-defined crystalline order. This characteristic which is partial melting before the melting point (premelting), is also called superionic state which has made this material a good superionic conductor. In general, superionic conductors, also known as fast-ion conductors, are multicomponent systems in which one of the ionic species rapidly diffuses below the melting point.[42] In this case, the material exhibits ionic conductivity in the solid phase which technologically facilitates its applications as electrolytes in fuel cells and solid-state batteries.[43,44] CaF_2, regarded as a typical ionic conductor, clearly displays such superionic behavior.[45] Such behavior has been observed just in those halids which crystallize in fluorite structure which could be a consequence of the availability of large octahedral empty spaces in this lattice. Such behavior of CaF_2 in bulk phase has been reported and studies by some groups.[45–48] Based on having such knowledge, the MD simulations of bulk phase were done according to the setting as was described in Sec. II B. From the crystallographic point of view, the crystal of CaF_2 consists of two sublattices, calcium ions (Ca^{+2}) arranged in a face-centered cubic structure and the fluorine ions (F^-) occupying the eight tetrahedral interstitial sites in the form of simple cubic sublattice. Therefore, each MD simulation was considered and analyzed according to the MSD of the Ca^{+2} and F^- separately. According to the behavior of MSD of each species as a function of temperature (see Fig. 6 for the selected temperatures), it was noticed that the F^- sublattice is thermally less stable than the Ca^{+2} sublattice which is in agreement of our prior knowledge. One reason of lower diffusivity of Ca^{+2} in comparison with F^- could be the more energetically costly of this ion due to its higher ionic charge relative to F^{-43}, which is also supported by direct measurements.[49] Beside that, based on the behavior of MSD of each chemical component of the system, the F$^-$ sublattice becomes disordered at temperatures higher than 1200 K which is again in agreement with the results of experimental and *ab initio* DFT-based MD simulations data presented by Cazrola *et al*[45] on CaF$_2$ in the cubic fluorite phase. In that study, the critical temperature for F$^-$ diffusivity was reported about 1400(90) K. On the basis of our MD simulations, the CENT potential provides a supeionic critical temperature of 1400 K, which is in good agreement with that experimental data and DFT calculations. Therefore, in general, we find the results of our MD simulations of bulk phase in good agreement with studies reported in literatures.

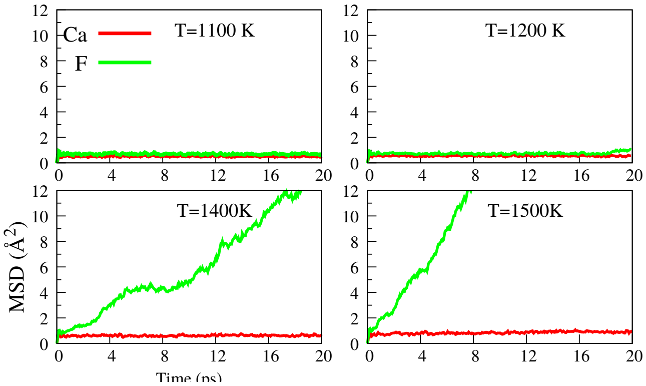

FIG. 6. (color online) Mean-squared displacement (MSD) of calcium ions (red lines) and fluorine ions (green lines) in bulk of CaF$_2$ at different temperatures as a function of simulation time.

The second test was done for the (111) surface. This surface was modeled with 12 atomic layers, which can also be interpreted as four layers of combined F-Ca-F triple layers (see Fig. 1 for the arrangements of layers). The perfectly flat (111) surface after cleaving from bulk is F$^-$ terminated, forming a hexagonal array on the surface. The dynamics and structure of this surface were investigated at different temperatures. The changes of MSD as a function of simulation time at different temperatures were considered in details for all the Ca^{+2} and F^- ions in the system (Fig. 7) as well as those in the first and second triplet layers (Fig. 8). According to such analyzes and visualizing the MD trajectories, it was noticed that in spite of increasing the atomic fluctuations due to increased temperature, the surface structure remains similar to the bulk-terminated structure. These results are in agreement with tensor LEED approach and MD simulations done by Gotte *et al.*[15] By counting the F^- and Ca^{+2} layers separately from the top of the surface, the reported values of MSD of the F1, Ca1, F2, F3, Ca2, and F4 resulting from the LEED in that study were 0.04±0.01, 0.020±0.006, 0.03±0.01, 0.014±0.007, 0.010±0.004, and 0.014±0.005 Å^2. In comparison with our obtained values from MD simulation for the same experimental temperature (See Fig. 8 for T=300 K) which are 0.0659, 0.0465, 0.0499, 0.0386, 0.0255, and 0.0330 Å^2, we find the values qualitatively in agreement with experiment. Quantitatively, we find the maximum and minimum absolute errors about 0.0265 and 0.0155 Å^2, respectively. So, the root mean squared error (RMSE) of the CENT potential is about 0.02 Å^2 which is very close to the the highest uncertainty of experimental data.

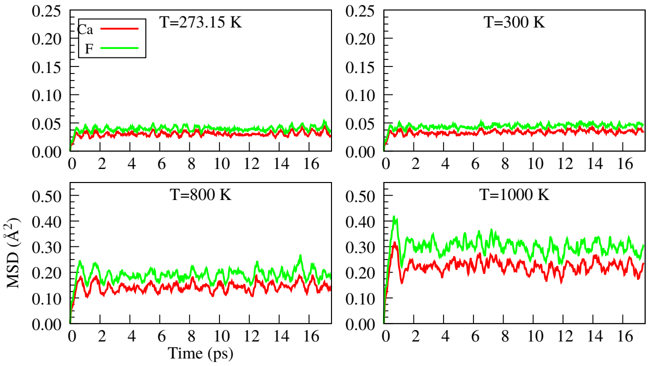

FIG. 7. (color online) Mean-squared displacement (MSD) of calcium ions (red lines) and fluorine ions (green lines) in (111) surface of CaF$_2$ at temperatures 273.15, 300, 800, and 1000 K as a function of simulation time.

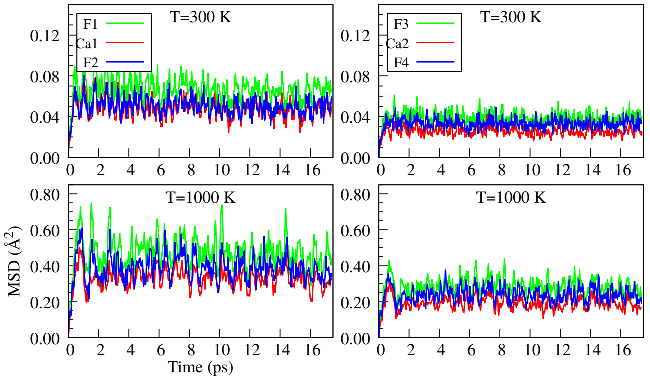

FIG. 8. (color online) Mean-squared displacement (MSD) for the two outermost F-Ca-F triple layers of (111) surface. The first and second columns illustrate the values for the first and second F-Ca-F triple layers, respectively at temperatures 300 and 1000 K.

Based on these two test sets, the CENT potential demonstrates reliable results and acceptable performance to predict properties at nonzero temperatures.

C. MD simulations of (100) surfaces

According to our studies and analyses, (111) and (110) are stable structures which are stable even at high temperatures. So in this part, we just represent the results of (100) surface. Fig 9 shows the MSD for the Ca^{+2} and

F^- ions at different temperatures as a function of simulation time. According to these plots, we could not see any diffusion for both types of ions at temperatures up to 600 K. Thus, no melting occurs at this range of temperature. Based on the plots, the Ca^{+2} sublattice keeps its stability and not obtaining any considerable diffusion upto temperatures lower than 900 K, indicating the stability of this sublattice. As illustrated in the plots, the melting transition of this sublattice occurs at T=900 K and as temperature increases, the sample becomes close to be completely disordered. In contrast to Ca^{+2}, the diffusion of F^- ions is considerable at temperatures around 600 K, indicating the melting of F^- sublattice. In conclusion, premelting occurs at temperatures around 600 K which is about three times smaller than the melting temperature of CaF_2 which is ≈ 1700 K.

In order to give further details about the diffusivity of the ions and their distributions on total MSD, the ions were considered according to their types and the layer in which they were placed. As shown in Fig. 1, the arrangement of atoms along [100] direction is alternative layers of F and Ca atoms, i.e. one layer F and one layer Ca^{+2}, resulting in 11 layers. Thus, the layers were considered separately by giving number 1 to 11, starting from the lowest layer which consists of F^- ions to the topmost layer which consists again of F^- ions. The left and right columns of Fig 10 show the MSD of Ca^{+2} and F^- ions, respectively. The key boxes indicate different layers, e.g. F-$la1$ in the figure means F^- ions in the bottom layer.

Considering just the MSD plots of Ca^{+2} ions in different layers and temperatures, it was noticed that at room temperature, there was not any diffusion of Ca^{+2} ions. However, by increasing temperature to those larger than 700 K, the value of MSD starts to increase and at T=900 K obtains a considerable value, mostly affected just by the outer layer of Ca^{+2} ions. This can be a sign of CaF_2 surface melting occurring at temperatures lower than 1200 K. As temperature increases more and more, the other layers also find considerable contributions in the increased MSD. The lowest panels illustrate that at temperatures higher than 1000 K, all the Ca^{+2} layers are affected and the sample is completely molten at T= 1500 K.

Considering the plots of F^- ions and comparing them with those obtained for Ca^{+2} ions at the same temperatures, demonstrates the higher mobility of F^- ions which is also in agreement with the less stability of this sublattice obtained for the bulk phase. Similar to Ca^{+2}, it was noticed that at room temperature the MSD was too small and negligible. By increasing temperature up to T=500 K, the F^- ions in the outer layers obtained a small displacements, higher than those of Ca^{+2} ions at the same temperature. Then at T=600K, the F^- ions in the outer layers were found mobile. They obtain considerable displacements while the Ca^{+2} ions are still more or less fixed at their initial positions, which consequently results in larger MSD of F ions. This procedure continues up to 1000 K, in which the central layers also start to be mobile. Thus, all the F^- layers contribute to MSD, while the Ca^{+2} layers have attained small movements. Therefore, the F^- sublattice is molten while the one for Ca^{+2} is still recognizable. As temperature continues to go above the 1000 K, the significant diffusion can be observed for all the layers, including both the central F and Ca layers. Consequently, the whole of the sample melts at temperatures higher than 1000 K, which is still below the melting temperature of the material in bulk phase.

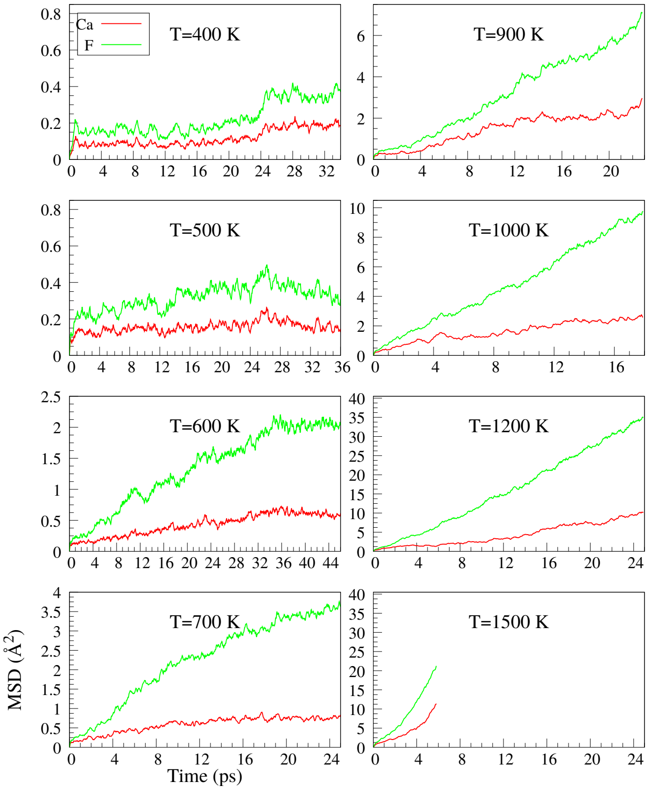

FIG. 9. (color online) MSD of calcium ions (red lines) and fluorine ions (green lines) in (100) surface of CaF$_2$ at different temperatures. UPDATE T1500 K.

IV. DISCUSSION AND CONCLUSIONS

The (111) and (110) surface are very stable and no significant surface reconstruction was observed for them during the structural search. On the other hand, the (100) surface represents a plethora of surface reconstructions. SHOULD BE ADDED LATER...

V. ACKNOWLEDGMENTS

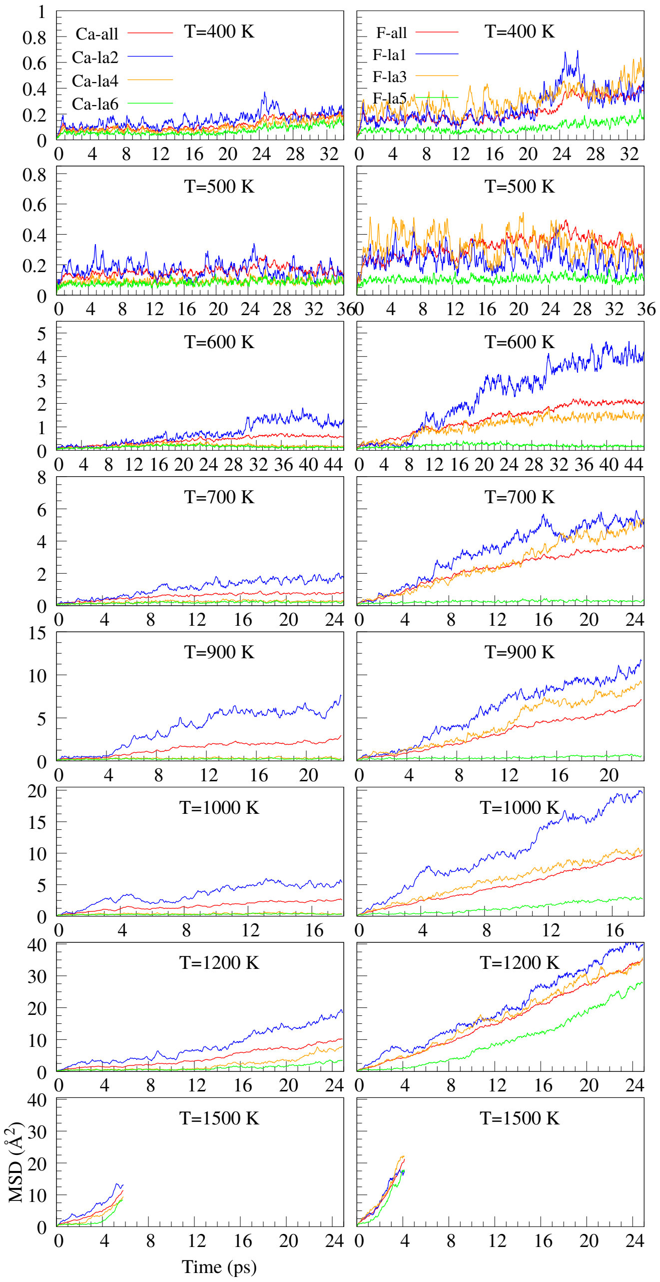

FIG. 10. (color online) MSD for the Ca and F layers of (100) surface at different temperatures as a function of simulation time. The first and second columns illustrate the values for the Ca and F layers, respectively

---

[*] aghasemi@iasbs.ac.ir

[1] K. Kelley and E. King, Mines Bull **584**, 126 (1960).
[2] B. Porter and E. Brown, Journal of the American Ceramic Society **45**, 49 (1962).
[3] V. Liberman, T. Bloomstein, M. Rothschild, J. Sedlacek, R. Uttaro, A. Bates, C. Van Peski, and K. Orvek, Journal of Vacuum Science & Technology B: Microelectronics and Nanometer Structures Processing, Measurement, and Phenomena **17**, 3273 (1999).
[4] M. Daimon and A. Masumura, Applied optics **41**, 5275 (2002).
[5] C. Wagner and N. Harned, Nature Photonics **4**, 24 (2010).
[6] W. Liang, V. Ilchenko, D. Eliyahu, A. Savchenkov, A. Matsko, D. Seidel, and L. Maleki, Nature communi-

cations **6**, 7371 (2015).

[7] X. C. Luo, J. N. Sun, W. L. Chang, and J. M. Ritchie, in *Key Engineering Materials*, Vol. 516 (Trans Tech Publ, 2012) pp. 408–413.

[8] L. Sang, M. Liao, Y. Koide, and M. Sumiya, Applied Physics Letters **98**, 103502 (2011).

[9] P. Tasker, Le Journal de Physique Colloques **41**, C6 (1980).

[10] V. Puchin, A. Puchina, M. Huisinga, and M. Reichling, Journal of Physics: Condensed Matter **13**, 2081 (2001).

[11] N. H. de Leeuw and T. G. Cooper, Journal of Materials Chemistry **13**, 93 (2003).

[12] J. Vogt, J. Henning, and H. Weiss, Surface science **578**, 57 (2005).

[13] R. Eglitis, H. Shi, and G. Borstel, Surface Review and Letters **13**, 149 (2006).

[14] S. Hirth, F. Ostendorf, and M. Reichling, Nanotechnology **17**, S148 (2006).

[15] A. Gotte, M. Baudin, A. Cabello-Cartagena, J. Vogt, and H. Weiss, Surface science **601**, 411 (2007).

[16] Z. Zhao-Yi, C. Xiang-Rong, Z. Jun, and H. Cui-E, Chinese Physics Letters **25**, 230 (2008).

[17] Y. Kakinuma, S. Azami, and T. Tanabe, CIRP Annals-Manufacturing Technology **64**, 117 (2015).

[18] L. Chen, L. Hu, C. Xiao, Y. Qi, B. Yu, and L. Qian, Wear **376**, 409 (2017).

[19] Y. Mizumoto and Y. Kakinuma, Precision Engineering (2018).

[20] Y. J. Lee, A. Chaudhari, J. Zhang, and H. Wang, in *Simulation and Experiments of Material-Oriented Ultra-Precision Machining* (Springer, 2019) pp. 77–102.

[21] Z. Gao, R. Fan, J. Ralston, W. Sun, and Y. Hu, Minerals Engineering **130**, 15 (2019).

[22] A. Pucci, J. Vogt, H. Weiß, and M. Reichling, Surface and Interface Science **3**, 279 (2013).

[23] E. Soares, V. B. Nascimento, V. De Carvalho, C. De Castilho, A. De Carvalho, R. Toomes, and D. Woodruff, Surface science **419**, 89 (1999).

[24] M. A. Vanhove, W. H. Weinberg, and C.-M. Chan, *Low-energy electron diffraction: experiment, theory and surface structure determination*, Vol. 6 (Springer Science & Business Media, 2012).

[25] F. Resende, V. Carvalho, B. Costa, and C. De Castilho, Brazilian journal of physics **34**, 414 (2004).

[26] M. Schick, H. Dabringhaus, and K. Wandelt, Surface science **592**, 42 (2005).

[27] S. Goedecker, J. Chem. Phys. **120**, 9911 (2004).

[28] M. Amsler and S. Goedecker, J. Chem. Phys. **133**, 224104 (2010).

[29] G. Fisicaro, M. Sicher, M. Amsler, S. Saha, L. Genovese, and S. Goedecker, Physical Review Materials **1**, 033609 (2017).

[30] J. O'neill, B. Redfern, and C. Brookes, Journal of Materials Science **8**, 47 (1973).

[31] S. A. Ghasemi, A. Hofstetter, S. Saha, and S. Goedecker, Physical Review B **92**, 045131 (2015).

[32] S. Faraji, S. A. Ghasemi, S. Rostami, R. Rasoulkhani, B. Schaefer, S. Goedecker, and M. Amsler, Physical Review B **95**, 104105 (2017).

[33] S. Plimpton, Journal of computational physics **117**, 1 (1995).

[34] L. Zhu, M. Amsler, T. Fuhrer, B. Schaefer, S. Faraji, S. Rostami, S. A. Ghasemi, A. Sadeghi, M. Grauzinyte, C. Wolverton, and S. Goedecker, J. Chem. Phys. **144**, 034203 (2016).

[35] W. A. Franke, European Journal of Mineralogy **27**, 255 (2015).

[36] J. P. Perdew, K. Burke, and M. Ernzerhof, Physical review letters **77**, 3865 (1996).

[37] L. Genovese, A. Neelov, S. Goedecker, T. Deutsch, S. A. Ghasemi, A. Willand, D. Caliste, O. Zilberberg, M. Rayson, A. Bergman, *et al.*, The Journal of chemical physics **129**, 014109 (2008).

[38] L. Genovese, B. Videau, M. Ospici, T. Deutsch, S. Goedecker, and J.-F. Méhaut, Comptes Rendus Mécanique **339**, 149 (2011).

[39] C. Hartwigsen, S. Gœdecker, and J. Hutter, Physical Review B **58**, 3641 (1998).

[40] E. Yakub, C. Ronchi, and D. Staicu, The Journal of chemical physics **127**, 094508 (2007).

[41] B. Schumann and H. Neumann, Crystal Research and Technology **19**, K13 (1984).

[42] C. Catlow and M. Norgett, Journal of Physics C: Solid State Physics **6**, 1325 (1973).

[43] S. Hull, Reports on Progress in Physics **67**, 1233 (2004).

[44] E. Kendrick and P. R. Slater, Annual Reports Section" A"(Inorganic Chemistry) **109**, 396 (2013).

[45] C. Cazorla and D. Errandonea, Physical review letters **113**, 235902 (2014).

[46] A. Annamareddy and J. Eapen, The Journal of chemical physics **143**, 194502 (2015).

[47] J. R. Nelson, R. J. Needs, and C. J. Pickard, Physical Review B **95**, 054118 (2017).

[48] J. R. Nelson, R. J. Needs, and C. J. Pickard, Physical Review B **98**, 224105 (2018).

[49] H. Matzke, Journal of Materials Science **5**, 831 (1970).